Test of Power Transformation Function to Hydrometeor and Water Vapor Mixing Ratios for Direct Variational Assimilation of Radar Reflectivity Data

JIAFEN HU,[a,b,d] JIDONG GAO,[b,d] CHENGSI LIU,[c] GUIFU ZHANG,[d] PAMELA HEINSELMAN,[b,d] AND JACOB T. CARLIN[a,b]

[a] *Cooperative Institute for Severe and High-Impact Weather Research and Operations, University of Oklahoma, Norman, Oklahoma*
[b] *NOAA/OAR/National Severe Storms Laboratory, Norman, Oklahoma*
[c] *Center for Analysis and Prediction of Storms, University of Oklahoma, Norman, Oklahoma*
[d] *School of Meteorology, University of Oklahoma, Norman, Oklahoma*

(Manuscript received 31 August 2022, in final form 24 July 2023, accepted 30 July 2023)

ABSTRACT: Assimilating radar reflectivity into convective-scale NWP models remains a challenging topic in radar data assimilation. A primary reason is that the reflectivity forward observation operator is highly nonlinear. To address this challenge, a power transformation function is applied to the WRF Model's hydrometeor and water vapor mixing ratio variables in this study. Three 3D variational data assimilation experiments are performed and compared for five high-impact weather events that occurred in 2019: (i) a control experiment that assimilates reflectivity using the original hydrometeor mixing ratios as control variables, (ii) an experiment that assimilates reflectivity using power-transformed hydrometeor mixing ratios as control variables, and (iii) an experiment that assimilates reflectivity and retrieved pseudo–water vapor observations using power-transformed hydrometeor and water vapor mixing ratios (q_v) as control variables. Both qualitative and quantitative evaluations are performed for 0–3-h forecasts from the five cases. The analysis and forecast performance in the two experiments with power-transformed mixing ratios is better than the control experiment. Notably, the assimilation of pseudo–water vapor with power-transformed q_v as an additional control variable is found to improve the performance of the analysis and short-term forecasts for all cases. In addition, the convergence rate of the cost function minimization for the two experiments that use the power transformation is faster than that of the control experiments.

SIGNIFICANCE STATEMENT: The effective use of radar reflectivity observations in any data assimilation scheme remains an important research topic because reflectivity observations explicitly include information about hydrometeors and also implicitly include information about the distribution of moisture within storms. However, it is difficult to assimilate reflectivity because the reflectivity forward observation operator is highly nonlinear. This study seeks to identify a more effective way to assimilate reflectivity into a convective-scale NWP model to improve the accuracy of predictions of high-impact weather events.

KEYWORDS: Radars/Radar observations; Numerical weather prediction/forecasting; Short-range prediction; Data assimilation

1. Introduction

Weather radar observations are very important for convective-scale NWP as they can provide information with sufficient temporal and spatial resolution to resolve convective storms (Lilly 1990). The assimilation of radar data into NWP models can greatly improve the analysis and forecasts of convective storms (Gao et al. 1999, 2016; Tong and Xue 2005; Hu et al. 2006a,b; Stensrud and Gao 2010; Carley 2012; Gao and Stensrud 2012, and many others). Most weather radars provide radial velocity and reflectivity observations. Radial velocity can be straightforwardly assimilated into convective-scale NWP models because of its linear and simple relationship with the three components of the model wind field. However, the assimilation of radar reflectivity into convective-scale NWP models is much more difficult (Gao and Stensrud 2012). Because of this, early studies usually adopted relatively simple or empirical methods for assimilating reflectivity into convective-scale NWP models. For example, complex cloud analysis schemes use radar reflectivity data directly to retrieve hydrometers and adjust in-cloud temperature and moisture (Hu et al. 2006a,b). Although the cloud analysis approach is efficient with a low computational cost, it can introduce model errors owing to its reliance on empirical relations between the adjusted variables and reflectivity.

Another way to assimilate radar reflectivity is to develop an observation forward operator that converts model-predicted variables (e.g., hydrometeor mixing ratios) to observed variables (i.e., radar reflectivity). Many different reflectivity forward operators have been developed and tested in both variational and ensemble-based data assimilation approaches (Xiao et al. 2007; Jung et al. 2008; Ryzhkov et al. 2011; Gao and Stensrud 2012; Wang et al. 2013; Wheatley et al. 2015; Zhang 2017; Wang and Wang 2017; Liu et al. 2019; Wang et al. 2019; Zhang et al. 2021). Although these studies demonstrated promising results, some challenges remain. Because of strong nonlinearity in the relationship between reflectivity and model-predicted variables, typical reflectivity forward operators have minimization difficulties if applied in any variational data assimilation approach.

Sun and Crook (1997) implemented a simple reflectivity forward operator, in which the relation between reflectivity

Corresponding author: Jidong Gao, Jidong.Gao@noaa.gov

DOI: 10.1175/WAF-D-22-0158.1

and rain mixing ratio is derived by assuming the Marshall–Palmer distribution of raindrop size, to assimilate reflectivity in their four-dimensional variational data assimilation scheme (4DVAR). They found that, when the background rainwater mixing ratio was very small, a very large cost function gradient occurred, resulting in difficulty reaching the minimization convergence when the simple reflectivity forward operator was used.

To address the nonlinearity problem of existing reflectivity forward operators, Carley (2012) assimilated radar reflectivity data using logarithmic transformations of retrieved hydrometeor mixing ratios as the control variables in the Gridpoint Statistical Interpolation (GSI) hybrid ensemble–3DVAR system. Liu et al. (2020) also proposed several treatments for alleviating nonlinearity issues using the 3DVAR method, which included using logarithmic mixing ratios as state variables with a lower limit threshold and background smoothing. Their results demonstrated that using logarithmic mixing ratios as control variables created analyses that were more consistent with observations, and that the convergence processes were faster. However, both studies found using logarithmic mixing ratios as state variables can introduce spurious cells.

Recently, Yang et al. (2020) adopted a nonlinear transformation function to improve the variational analysis of visibility and cloud ceiling height, based on NCEP's Real-Time Mesoscale Analysis (RTMA) system. This newly proposed power transformation function can make non-Gaussian variables more normally distributed. Additionally, the transformation function can range from linear to logarithmic by varying a parameter from 1 to 0, respectively. In a more recent study, the idea of applying a power transformation to control variables was used for reflectivity data assimilation by treating the retrieved hydrometeor variables as control variables (Chen et al. 2021; Li et al. 2022). Results showed that the assimilation of reflectivity with this transformation function gave the best short-term severe weather forecasts compared to either no transformation or a logarithmic transformation function. This approach is promising but has yet to be extensively explored.

In this study, we further investigate the degree to which the application of this power transformation function to hydrometeor mixing ratios as control variables is useful for convective-scale NWP. In addition, we apply the power transformation function to water vapor mixing ratio to test whether the retrieved pseudo–water vapor (Lai et al. 2019) can also be effectively assimilated into the system. The efficiency of a data assimilation scheme is essential for real-time forecasting applications. Severe convective weather events, which are characterized by local, sudden, and short life cycles, require fast and timely forecasts, early warnings, and the quick delivery of these forecasts and warnings to the public (Zhao et al. 2021). Thus, a three-dimensional variational data assimilation method developed for convective-scale NWP (Gao et al. 2013) is used due to its low computational cost. However, it is expected that the overall conclusions drawn using 3DVAR in this study will remain valid for other advanced data assimilation methods, such as 3DEnVAR, 4DVAR, and so on (Caya et al. 2005; Tong and Xue 2005; Gao and Xue 2008; Sun and Wang 2013; Yussouf et al. 2013; Johnson et al. 2015), as they have the same issue regarding how to effectively deal with highly nonlinear reflectivity operators. A brief description of this method is provided in the next section.

The remainder of this work is organized as follows. Section 2 briefly describes the 3DVAR analysis and forecast system implementation. It also discusses the methodology, including the 3DVAR system, radar forward operators, power transformation function, and pseudo–water vapor retrieval. The experiment design is detailed in section 3, followed by a presentation of the results in section 4. Section 5 concludes with a summary and discussion of considerations for future work.

2. Methodology

a. The 3DVAR system

The overarching principle of variational data assimilation techniques is to find the best analysis for NWP by minimizing a cost function (Lorenc 1986). The following formulation of a 3DVAR cost function was proposed by Gao et al. (2004):

$$J(\mathbf{x}) = \frac{1}{2}(\mathbf{x} - \mathbf{x}^b)^{\mathrm{T}}\mathbf{B}^{-1}(\mathbf{x} - \mathbf{x}^b) + \frac{1}{2}[H(\mathbf{x}) - \mathbf{y}^o]^{\mathrm{T}}\mathbf{R}^{-1}[H(\mathbf{x}) - \mathbf{y}^o] + J_c(\mathbf{x}). \quad (1)$$

The first term on the right-hand side of the equation measures the distance between the analysis or control vector $\mathbf{x}$ and the background vector $\mathbf{x}^b$, and is weighted by the inverse of the background error covariance matrix $\mathbf{B}$. The 3DVAR system assimilates radar radial velocity, reflectivity, and surface observations. Thus, there are several variables included in the analysis vector $\mathbf{x}$: the wind components (u, v, and w), the hydrometeor mixing ratios for rainwater (q_r), snow (q_s), and hail (q_h), potential temperature (θ), and water vapor mixing ratio (q_v).

The second term of the cost function is the observation term, which determines the distance between the analysis vector $\mathbf{x}$ mapped to the observation variables and locations by the forward observation operator $H(\mathbf{x})$, and the observation vector $\mathbf{y}^o$, and that is weighted by the inverse of the observation error covariance matrix $\mathbf{R}$. The third term $J_c(\mathbf{x})$ is a penalty term that employs the mass continuity equation as a weak constraint (Gao et al. 1999, 2004).

To effectively precondition the minimization problem, we follow Courtier et al. (1994) and Courtier (1997) and define an alternative control variable $\mathbf{v}$, such that $\mathbf{C} = \sqrt{\mathbf{B}}\mathbf{v} = (\mathbf{x} - \mathbf{x}^b)$. This allows the cost function (1) to be changed into an incremental form, such that

$$J_{\mathrm{inc}}(\mathbf{v}) = \frac{1}{2}\mathbf{v}^{\mathrm{T}}\mathbf{v} + \frac{1}{2}(\mathbf{HC} - \mathbf{d})^{\mathrm{T}}\mathbf{R}^{-1}(\mathbf{HC} - \mathbf{d}) + J_c(\mathbf{v}), \quad (2)$$

where $\mathbf{H}$ is the linearized version of H and $\mathbf{d} \equiv \mathbf{y}^o - H(\mathbf{x}^b)$. The gradient and Hessian of J_{inc} can also be derived by differentiating (2) with respect to $\mathbf{v}$, yielding

$$\nabla J_{\mathrm{inc}} = (\mathbf{I} + \mathbf{C}^{\mathrm{T}}\mathbf{H}^{\mathrm{T}}\mathbf{R}^{-1}\mathbf{HC})\mathbf{v} - \mathbf{C}^{\mathrm{T}}\mathbf{H}^{\mathrm{T}}\mathbf{R}^{-1}d + \nabla J_c(\mathbf{v}), \quad (3)$$

where $\mathbf{I}$ is the identity matrix. The Hessian then follows as

$$\nabla^2 J_{\text{inc}} = \mathbf{I} + \mathbf{C}^{\mathrm{T}}\mathbf{H}^{\mathrm{T}}\mathbf{R}^{-1}\mathbf{H}\mathbf{C} + \nabla^2 J_c(\mathbf{v}). \quad (4)$$

The preconditioning in (4) prevents the smallest eigenvalue from becoming close to zero. This can improve convergence of minimization algorithms and allows the variational problem to be solved more efficiently.

b. Radar forward observation operator

The radar forward observation operator H transforms model state variables (e.g., u, v, q_r, q_s) in model space to observational measurements in observation space (e.g., radial velocity, reflectivity). Both radar radial velocity and reflectivity are assimilated within the 3DVAR framework in this study. The details of the radial velocity and reflectivity forward observation operators are described as follows.

Radar radial velocity data are part of the observation vector $\mathbf{y}^o$ in Eq. (1). The radar forward observation operator for radial velocity, which includes the effects of Earth's curvature, is written as follows in Doviak and Zrnić (1993):

$$v_r = \frac{dh}{dr}w + \frac{ds}{dr}(u\sin\phi + v\cos\phi), \quad (5)$$

where v_r is the projected radial velocity; and u, v, and w are the zonal, meridional, and vertical components of the wind, respectively; r is the slant range (ray path distance); h is the height above the curving Earth's surface; s is the distance along Earth's surface; and φ is the azimuth angle of the radar beam direction.

The forward observation operator for radar reflectivity (Z, in dBZ) can be written as follows:

$$Z = 10\log_{10}(Z_e), \quad (6)$$

where Z_e is the equivalent radar reflectivity factor in linear units (mm^6 m^{-3}) obtained from the sum of the three simulated hydrometeor species (rainwater, snow, and hail), according to the following formulation (Dowell et al. 2011; Gilmore et al. 2004; Lin et al. 1983):

$$Z_e = Z_e(q_r) + Z_e(q_s) + Z_e(q_h). \quad (7)$$

In Eq. (7), $Z_e(q_r)$, $Z_e(q_s)$, and $Z_e(q_h)$ represent the equivalent radar reflectivity factors contributed from rainwater (q_r), snow (q_s), and hail (q_h), respectively. Based on Smith et al. (1975), each hydrometeor's contribution to reflectivity can be calculated from

$$Z_e(q_r) = 3.63\times10^9(\rho q_r)^{1.75}, \quad (8)$$

$$Z_e(q_s) = 9.80\times10^8(\rho q_s)^{1.75}\ (\text{dry snow},\ T\le 0°\text{C}), \quad (9)$$

$$Z_e(q_s) = 4.26\times10^{11}(\rho q_s)^{1.75}\ (\text{wet snow},\ T> 0°\text{C}), \quad (10)$$

$$Z_e(q_h) = 4.33\times10^{10}(\rho q_h)^{1.66}, \quad (11)$$

where ρ is the air density. The radar reflectivity forward observation operators mentioned above are highly nonlinear which may cause a large gradient of the cost function when background mixing ratios are very small (Sun and Crook 1997; Liu et al. 2020).

Equations (6)–(11) indicate the reflectivity factor is a function of all three hydrometeor variables (rainwater, snow, hail). This leads to the solution being underdetermined (Gao and Stensrud 2012). To solve this problem, Eq. (7) is further modified as

$$Z_e = \begin{cases} Z(q_r) & T_b > 5°\text{C} \\ Z(q_s) + Z(q_h) & T_b < -5°\text{C} \\ \alpha Z(q_r) + (1-\alpha)[Z(q_s) + Z(q_h)] & -5°\text{C} < T_b < 5°\text{C} \end{cases}, \quad (12)$$

where α varies linearly between 0 at $T_b = -5°$C and 1 at $T_b = 5°$C, and T_b is the background temperature from the WRF Model. Here, a priori partitioning of the hydrometeor variables in Eq. (12) allows the model background temperature to guide how much of the correction should occur in q_r compared to how much correction should occur in q_s and q_h (Gao and Stensrud 2012).

c. Power transformation function

Yang et al. (2020) proposed a nonlinear power transformation function to improve variational analysis of visibility and ceiling height. This power transformation function is applied to the hydrometeor and water vapor mixing ratios (q_r, q_s, q_h, q_v) and is defined as follows:

$$\hat{q} = \frac{(q^p - 1)}{p}\ (0 < p \le 1), \quad (13)$$

where $\hat{q}$ denotes the power-transformed mixing ratios and p represents a parameter which is larger than zero and smaller than or equal to 1. When p equals 1, this equation becomes

$$\hat{q} = q - 1, \quad (14)$$

which is a linear relationship between q and $\hat{q}$. The nonlinearity of the equation grows as the value of p decreases. When p approaches zero, this transformation function becomes a natural logarithm function. Thus, this nonlinear power transformation allows for a range of possible transformation functions, including both linear and logarithmic functions at each end of the parameter range.

Therefore, the equivalent reflectivity factor for rainwater after the power transformation can be written as follows:

$$Z_e(\hat{q}_r) = 3.63\times10^9[\rho(p\hat{q}_r + 1)^{1/p}]^{1.75}. \quad (15)$$

In addition, $\hat{q}$ needs to be greater than $-1/p$ to avoid negative values of hydrometeor mixing ratios when transforming back to the standard space. For other hydrometeors, the formulations are similar.

Chen et al. (2021) and Li et al. (2022) examined the performance of using power-transformed hydrometeor mixing ratios as control variables with different p values. Results indicated that $p = 0.4$ yielded the best 1-h reflectivity forecasts. Thus,

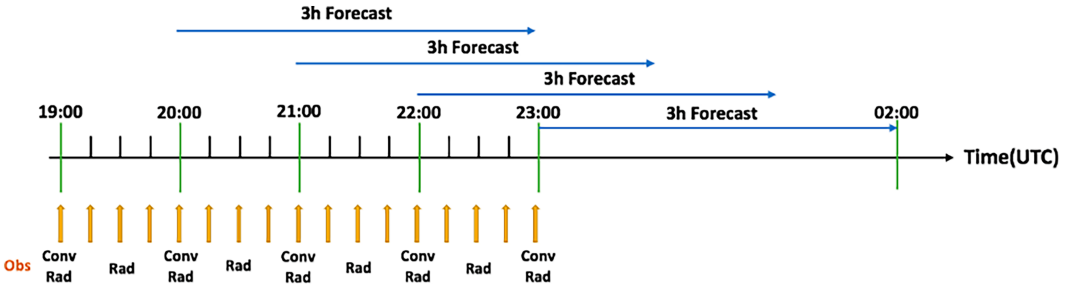

FIG. 1. Illustration of cycled data assimilation and forecast experiments. "Obs" represents the assimilated observations including conventional observations (Conv) and radar observations (Rad). The yellow arrows show the times when the observations are assimilated. The radar observations are assimilated every 15 min while the conventional observations are assimilated every hour.

we choose $p = 0.4$ in this study to test the power transformation function.

d. *Pseudo–water vapor mixing ratio observations*

Our recent studies have found that the assimilation of pseudo–water vapor, along with radar radial velocity and reflectivity, improved the analyses and forecasts of convective storms (Carlin et al. 2017; Lai et al. 2019). In this current study, the pseudo–water vapor mixing ratio observations are produced based on vertically integrated liquid water, which is derived from reflectivity observations (Lai et al. 2019). The detailed procedure can be found in that paper. To improve the efficiency of minimization, the power transformation function discussed in section 2c is also applied to the pseudo–water vapor as a control variable.

3. Experimental design

To test the impact of the power transformation function on the assimilation of radar data within the 3DVAR framework, five real-data cases with severe weather events (17, 20, 22, 23, and 28 May 2019) are selected from the 2019 Warn-on-Forecast (WoF) spring experiments (Clark et al. 2020). The forecast model employed in this study is the WRF-ARW Model version 3.7.1, which uses the following physics configuration: the Thompson microphysics scheme (Thompson et al. 2008), the Yonsei University (YSU) planetary boundary layer scheme (Hong et al. 2006), the Rapid Radiative Transfer Model for Global circulation models (RRTMG) shortwave and longwave schemes (Iacono et al. 2008), and the unified Noah land surface model (Tewari et al. 2004). The experiment domains for all the cases in this study have 600 × 600 grid points in the horizontal with a grid spacing of 1.5 km, and 51 vertical levels. The model top height is set to 50 hPa.

The flowchart of the cycled data assimilation and forecast experiments is shown in Fig. 1. For all five cases, the severe weather events occurred primarily between 1800 and 2300 UTC. The experiments are started at 1900 UTC and extend to 2300 UTC with the 3-km High-Resolution Rapid Refresh (HRRR) forecast fields providing the initial background for the data assimilation cycles and the lateral boundary conditions for forecasts. For each case, the radar observations downloaded from the NEXRAD Level-II data repository at the National Centers for Environmental Information (https://www.ncdc.noaa.gov/nexradinv/) are assimilated every 15 min during the 4-h cycling period, and the conventional observations (e.g., soundings, surface stations) are assimilated hourly at 1900, 2000, 2100, 2200, and 2300 UTC. Starting from 2000 UTC, 3-h forecasts are launched hourly until 2300 UTC. The gridded Multi-Radar Multi-Sensor (MRMS) composite radar reflectivity dataset (Smith et al. 2016) and the National Centers for Environmental Prediction (NCEP) Stage-IV hourly precipitation dataset (Du 2011) are used to verify the performance of the reflectivity and precipitation forecasts in this study.

Three types of experiments, labeled Q, PQ, and PQ_Pqv, are performed for each case. Detailed descriptions of the experiments are provided in Table 1. Radial velocity is assimilated the same way in all experiments. Experiment Q serves as the control experiment by assimilating radar reflectivity using the original hydrometeor variables as part of the control variables, but without assimilating pseudo–water vapor. Experiment PQ uses the power-transformed hydrometeors as part of the control variables but without assimilating water vapor. Finally, experiment PQ_Pqv uses power-transformed hydrometeors and pseudo–water vapor as control variables, with the assimilation of both radar data and pseudo–water vapor observations. These three experiments are compared to investigate the impact of the power transformation function on short-term convective-scale severe weather forecasts within the variational data assimilation framework.

TABLE 1. Description of experiments.

Expt name	Water-related variables	Description
Q	q	Expt with q_r, q_s, and q_h as control variables
PQ	Pq	Expt with power-transformed q_r, q_s, and q_h as control variables
PQ_Pqv	Pq, Pqv	Expt with power-transformed q_r, q_s, q_h, and q_v as control variables

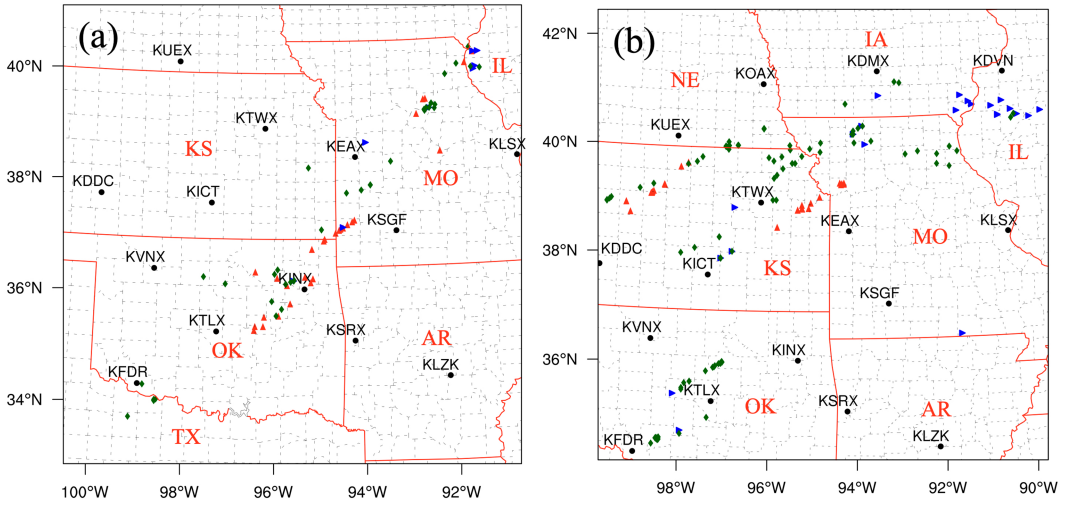

FIG. 2. The simulation domain and locations of the radar sites for (a) 22 May 2019 and (b) 28 May 2019. The red triangles, green rhombuses, and blue triangles indicate the observed tornadoes, hail, and wind events from Storm Prediction Center (SPC) storm reports, respectively.

Two severe weather cases are selected for more detailed analysis in the next section: the 22 May 2019 tornadic supercell storms in northeastern Oklahoma (the worst-performing case denoted as Case 1, Fig. 2a) and the 28 May 2019 tornado outbreak over the border of eastern Kansas and Missouri (one of the best-performing cases denoted as Case 2, Fig. 2b). The geographical center of the model simulation domains for these two cases are at 37.09°N, 95.60°W and 38.42°N, 94.75°W, respectively.

4. Results

a. 22 May 2019 case

The first case selected for this study occurred on 22 May 2019. Environmental conditions were favorable for the development of tornadoes and severe thunderstorms across northeast Oklahoma and Missouri. Early in the afternoon, isolated intense thunderstorms existed in southwest and central Oklahoma. Thunderstorms developed across northeast Oklahoma, southeast Kansas, and central and southwest Missouri that produced several tornadoes and widespread large hail (3 in. in diameter based on local NWS reports). The storms then spread northeastward through the evening and persisted into the early overnight period before weakening. In all, 47 tornadoes were reported ranging from EF0 to EF3, with 16 of them occurring in Oklahoma. The simulation domain for 22 May 2019 case includes most of Kansas, Oklahoma, Arkansas, and Missouri (Fig. 2a).

The analysis and forecast composite reflectivity fields from Q, PQ, and PQ_Pqv for the 3-h forecast initiated at 2300 UTC and the corresponding observed composite reflectivity fields are shown in Fig. 3. The convective cells within the simulation domain are divided into three main regions (labeled A, B, and C) to better illustrate the comparisons. At the analysis time (valid at 2300 UTC), the reflectivity patterns of all three experiments are similar to the observed composite reflectivity fields (Fig. 3a) in terms of storm locations. However, the storm intensity differs between each experiment. The storm cells in region A from PQ and PQ_Pqv (Figs. 3c,d) are stronger than that of Q (Fig. 3b), and are more consistent with the observations (Fig. 3a). The analyzed reflectivity field for PQ_Pqv (Fig. 3d) indicates that a cluster of several convective cells in region B is more vigorous than that for Q and PQ (Figs. 3b,c, respectively), also in better agreement with the observed reflectivity fields. Moreover, the weak cell in region C is closest to the observations for PQ_Pqv, in terms of pattern and intensity.

Although using power-transformed hydrometeor and water vapor mixing ratios as control variables produces more consistent analyses of reflectivity fields, the benefits do not persist in the forecasts, especially after one hour. At 1 h into the forecast (0000 UTC), the west-most cells in region B, and the weak cell in region C, decay very quickly for Q and PQ (Figs. 3f,g), though they are relatively better maintained for PQ_Pqv. The cell in region C completely dissipates for Q and PQ, but still exists for PQ_Pqv (though weaker than that observed, Fig. 3h). By 3 h, the forecasts for all three experiments are quite similar (Figs. 3n–p).

To further evaluate the usefulness of power transformation functions applied to hydrometeor and water vapor mixing ratios used as control variables, the maximum 2–5-km updraft helicity (UH) swaths for the 0–3-h forecasts initiated at 2300 UTC are overlaid with the Storm Prediction Center (SPC) storm reports in the simulation domain (Fig. 4). From the forecast beginning at 2300 UTC, the UH tracks for all three experiments (Figs. 4a–c) are similar but miss the supercells in northeast Oklahoma, which produced severe weather including tornadoes and hail reports. For the storm cells on the border of Missouri and Illinois, there is a southward bias for all experiments (Figs. 4a–c). However, the predicted UH tracks over the Oklahoma/Missouri border are stronger for PQ_Pqv (Fig. 4c) compared to Q (Fig. 4a) and PQ (Fig. 4b). Moreover,

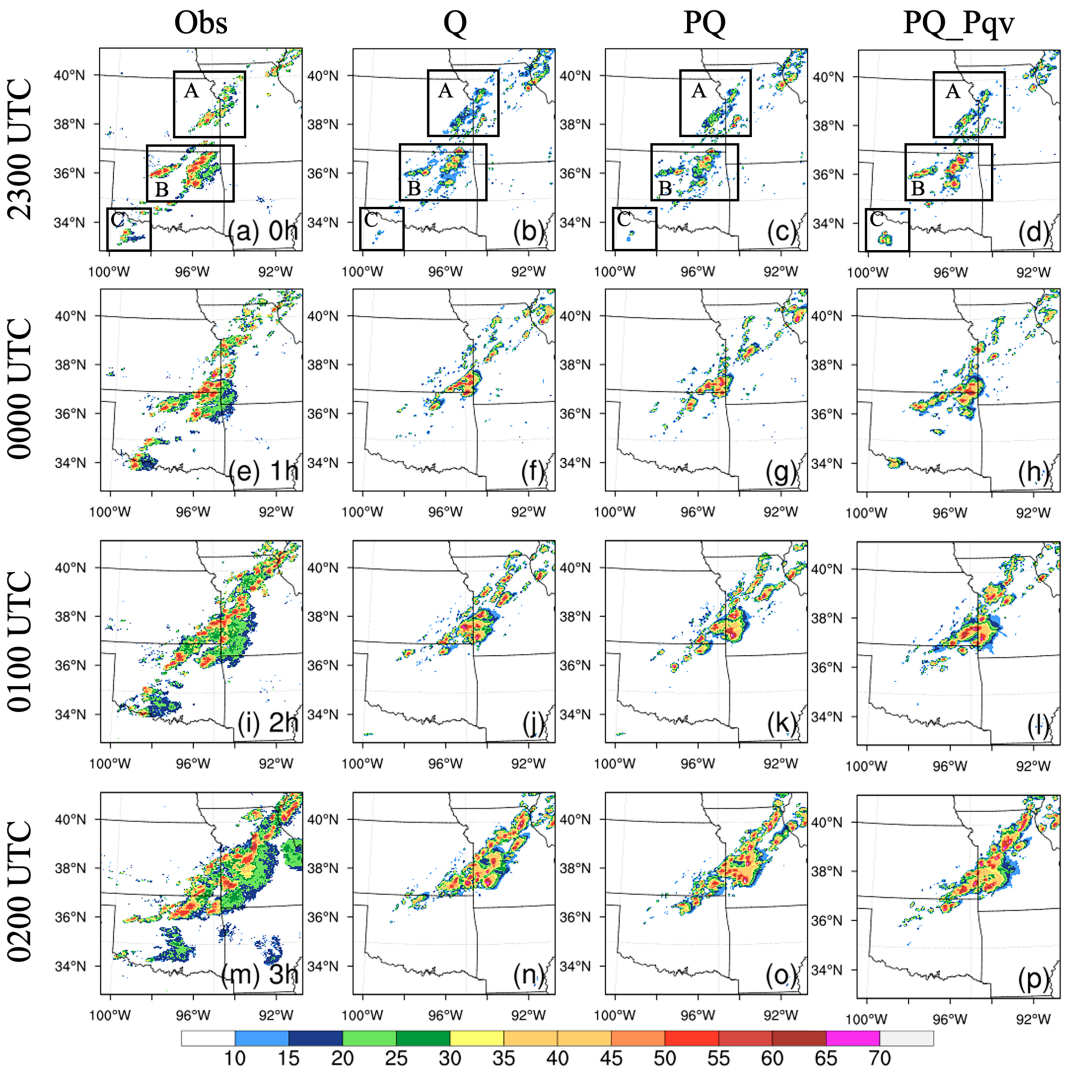

FIG. 3. (first column) The observed composite reflectivity and corresponding 3-h forecasts initiated at 2300 UTC 22 May 2019 from experiments (second column) Q, (third column) PQ, and (fourth column) PQ_Pqv. Plots are shown for the analysis time at (a)–(d) 2300 UTC, (e)–(h) the 1-h forecast valid at 0000 UTC, (i)–(l) 2-h forecast valid at 0100 UTC, and (m)–(p) 3-h forecast valid at 0200 UTC.

the mesoscale convective systems in northern Missouri for PQ_Pqv generate stronger UH tracks than in Q and PQ.

Figure 5 presents the 3-h accumulated precipitation forecasts initiated at 2300 UTC for Q, PQ, and PQ_Pqv. All experiments show similar precipitation forecast patterns for areas located on the border of Oklahoma and Kansas, and the border of Missouri and Kansas. The precipitation forecast in west-central Missouri for PQ_Pqv (red circle in Fig. 5d) is more consistent with the observations (Fig. 5a) in both intensity and areal coverage compared to Q (Fig. 5b) and PQ (Fig. 5c). However, the precipitation intensity is overestimated for PQ_Pqv in the southeast corner of Kansas. PQ_Pqv captures the weak rainfall near the boundary of Texas and Oklahoma, while both Q and PQ miss it.

Performance diagrams (Roebber 2009) are plotted to quantify the overall performance of the analysis and forecast resulting from the use of different control variables. The probability of detection (POD), bias, critical success index (CSI) and false alarm ratio (FAR) or its equivalent, success ratio (SR = 1 − FAR) are all included in the performance diagrams. The performance diagrams for the 3-h forecasts initiated at 2300 UTC for 20-, 30-, and 40-dBZ thresholds are shown in Fig. 6. The closer the values of POD, CSI, and SR are to unity, the better the forecast is. Therefore, the upper right corner of the diagram indicates a perfect forecast. At the analysis time, although the POD value of PQ and PQ_Pqv is slightly lower than that of Q at the threshold of 20 dBZ (Fig. 6a), they are much higher than that of Q at the 30- and 40-dBZ thresholds. PQ and PQ_Pqv produce higher CSI and SR at all reflectivity thresholds indicating improvement of the analysis when using power-transformed control variables (Fig. 6). Additionally, PQ_Pqv outperforms PQ with higher SR and CSI values at the 30- and 40-dBZ thresholds at analysis time (Figs. 6b,c). It is found that Q performs better than

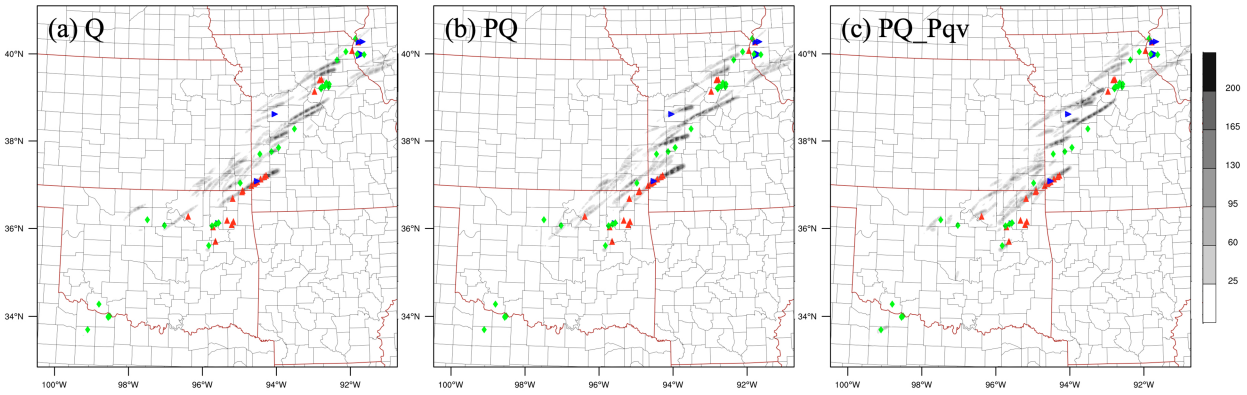

FIG. 4. The maximum 2–5-km updraft helicity track swaths ($m^2 s^{-2}$): (a) Q, (b) PQ, and (c) PQ_Pqv for the 0–3-h forecasts initiated at 2300 UTC 22 May 2019. The green rhombuses and red and blue triangles represent hail, tornadoes, and damaging winds from SPC reports, respectively.

PQ, but PQ_Pqv outperforms both Q and PQ at the 1-h forecast at all thresholds. For 2- and 3-h forecasts, the results are a little complicated. PQ_Pqv outperforms both Q and PQ at the 3-h forecast in terms of POD and CSI at all thresholds, and at the 2-h forecast in terms of POD at 20 and 30 dBZ. All three experiments exhibit similar performance for the 40-dBZ threshold at the 2- and 3-h forecasts. Generally, PQ_Pqv produces the best performance for the entire forecast period with the highest values of POD, SR, and CSI, especially at the 1-h forecast.

To compare the convergence rates of Q, PQ, and PQ_Pqv, the total and separate observational (i.e., radial velocity and reflectivity) cost functions normalized by their respective initial values are calculated for the 1900 UTC 22 May 2019 analysis as an example (Fig. 7). It is demonstrated that PQ and PQ_Pqv have faster convergence rates than Q during the minimization process with smaller cost function values, especially for the total and radial velocity cost functions (Figs. 7a,b). Because of the reduction of the nonlinearity of the cost function, the overall balance among different control variables during the minimization process becomes better and the analysis for winds improves significantly (Chen et al. 2021). For the reflectivity cost functions (Fig. 7c), all three experiments exhibit very similar convergence rates. This indicates that the use of a power transformation of hydrometeors as control variables has little impact on the convergence of the reflectivity cost function but does have an impact on the overall convergence of the minimization process. Note some small spikes exist in the cost function during the minimization process which may be caused by the complicated nonlinear problem in the cost function (Navon and Legler 1987; Li et al. 1994; Gao et al. 2001).

b. 28 May 2019 case

The second case occurred on 28 May 2019. Initially that afternoon, there was a slow-moving front draped from northeastern Kansas into northern Missouri. Storms formed and moved northeastward along this front. Scattered supercells also developed along the dryline from west-central Oklahoma northward into central Kansas, which favored the development of very large hail and tornadoes. The ongoing elevated thunderstorms persisted for several hours, and isolated severe storms formed and moved eastward across west central Kansas through the evening. These storms produced several tornadoes. Eventually, an EF4 tornado formed with estimated maximum winds of 170 mph. In all, 35 tornadoes were reported ranging from EF0 to EF4, with 21 tornadoes occurring in Kansas. The simulation domain of the experiments for 28 May 2019 case includes most of Oklahoma, Kansas, Missouri, Arkansas, Iowa, and Illinois (Fig. 2b).

Similar to the first case, Q, PQ, and PQ_Pqv are compared to examine the usefulness of applying the power transformation function to different control variables. The analyzed and forecast composite reflectivity fields for the 3-h forecasts initiated at 2200 UTC for the three experiments Q, PQ, and PQ_Pqv and the corresponding observed composite reflectivity fields are plotted (Fig. 8). Like in Case 1, the three main convection regions from north to south are marked and labeled as A, B, and C to better illustrate the comparisons (Fig. 8a). At the analysis time (valid at 2200 UTC), the reflectivity patterns of all three experiments are similar to the observed composite reflectivity in term of storm locations. However, the storm intensity differs in each experiment. The intensity of the cell in region A for PQ and PQ_Pqv (Figs. 8c,d) is closer to the observations compared with that of Q (Fig. 8b), especially on the border of Iowa and Missouri. The analyzed reflectivity fields for PQ (Fig. 8c) and PQ_Pqv (Fig. 8d) indicate that the convective cells in region B for both experiments are more vigorous than that for Q (Fig. 8b), in better agreement with the observed reflectivity fields. Moreover, a cluster of several storm cells in region C from PQ and PQ_Pqv are also stronger compared to Q, which is more consistent with the observations. A weak spurious cell is produced in Q in southeastern Kansas, which is reduced in both PQ and PQ_Pqv.

At the 1-h forecast (valid at 2300 UTC), a convective cell is predicted in region A for both PQ and PQ_Pqv (Figs. 8g,h), which is absent from Q (Fig. 8f). In addition, there are several storm cells predicted in the right and bottom-left portions of

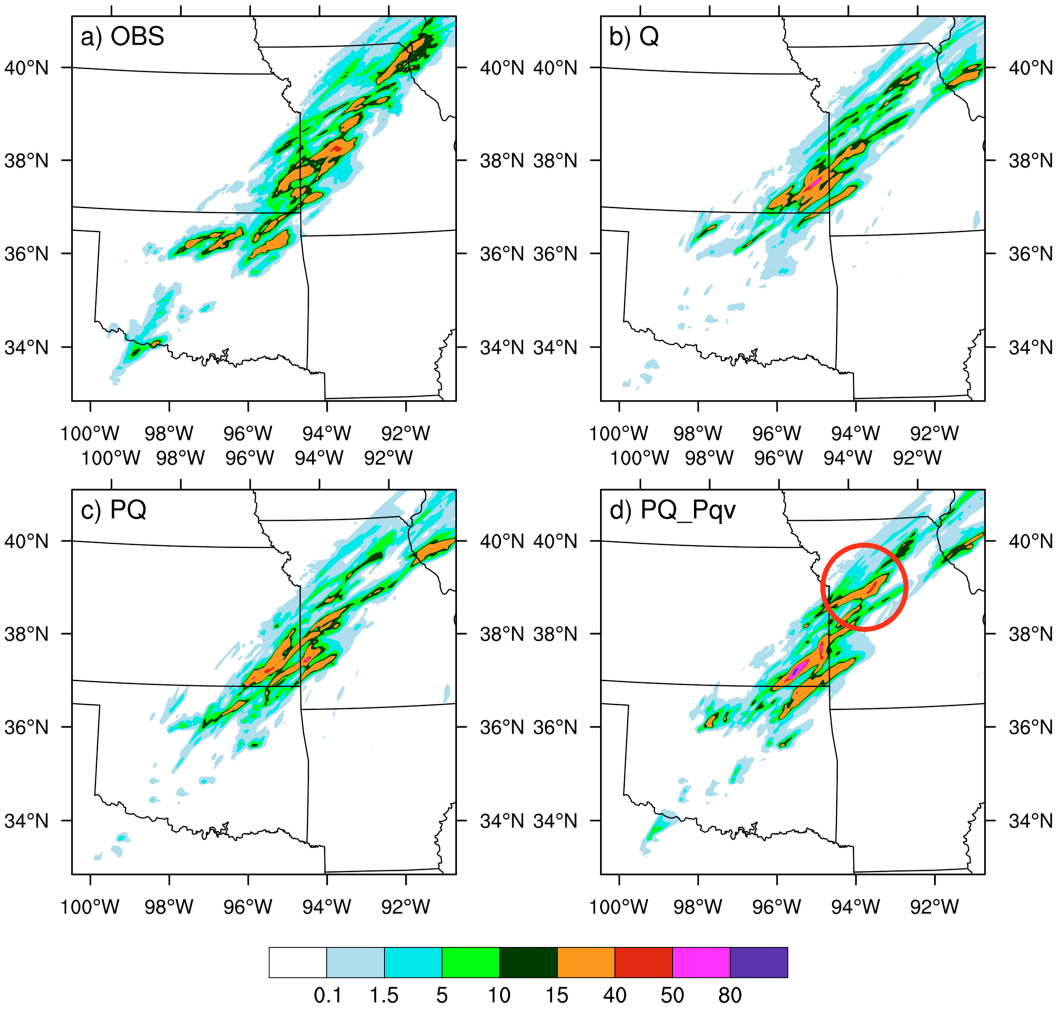

FIG. 5. The 3-h accumulated precipitation (mm) for NCEP Stage-IV (a) observations, (b) Q, (c) PQ, and (d) PQ_Pqv, initiated at 2300 UTC 22 May 2019. The red circle in (d) highlights the precipitation area in west-central Missouri.

region C for PQ_Pqv, which were not well-predicted in Q and PQ. By the 2-h forecast, the storm cell in region A is marginally predicted in both PQ and PQ_Pqv, but not for Q. However, the convective cells in the eastern portion of region C dissipate for all experiments (Fig. 8l). At 3 h into the forecast, all three forecasts look quite similar (Fig. 8p). Overall, the Q and PQ experiments exhibit very similar forecast performance based on the composite reflectivity fields. PQ_Pqv gives the best forecast performance, especially for the 1- and 2-h forecasts.

The maximum 2–5-km UH track swaths for the 0–3-h forecasts initiated at 2200 UTC are also calculated (Fig. 9). Similar to Case 1, the patterns of UH tracks are similar for all the experiments from the forecast initialized at 2200 UTC (Figs. 9a–c). In addition, the three experiments all exhibit an obvious northward bias, especially for the storm tracks in central and northern Oklahoma and central Kansas. However, a few distinguished discrepancies exist among the three experiments. The predicted UH swaths over the Kansas–Missouri and Kansas–Nebraska border are stronger and more consistent with the tornado reports for PQ_Pqv (Fig. 9c), with smaller phase errors and stronger intensities, compared with that of Q (Fig. 9a) and PQ (Fig. 9b). Moreover, the intensities of the UH tracks for PQ_Pqv are stronger than that of Q and PQ in central and northern Oklahoma. This further demonstrates the usefulness of applying a power transformation to hydrometeors used as control variables and the additional assimilation of pseudo–water vapor.

Figure 10 shows the 3-h accumulated precipitation forecasts initiated at 2200 UTC. The precipitation near the boundary of Missouri and Iowa are underpredicted in all three experiments with clear westward biases although PQ_Pqv has the best forecast in terms of areal coverage. At the border of Kansas and Nebraska, the forecast for PQ_Pqv (Fig. 10d) matches the observations better than that of Q (Fig. 10b) and PQ (Fig. 10c). Moreover, the two narrow precipitation bands in central Oklahoma are well captured in PQ_Pqv, which are underpredicted in Q and PQ compared with the observations (Fig. 10a). In general, PQ_Pqv shows better precipitation forecasts performance.

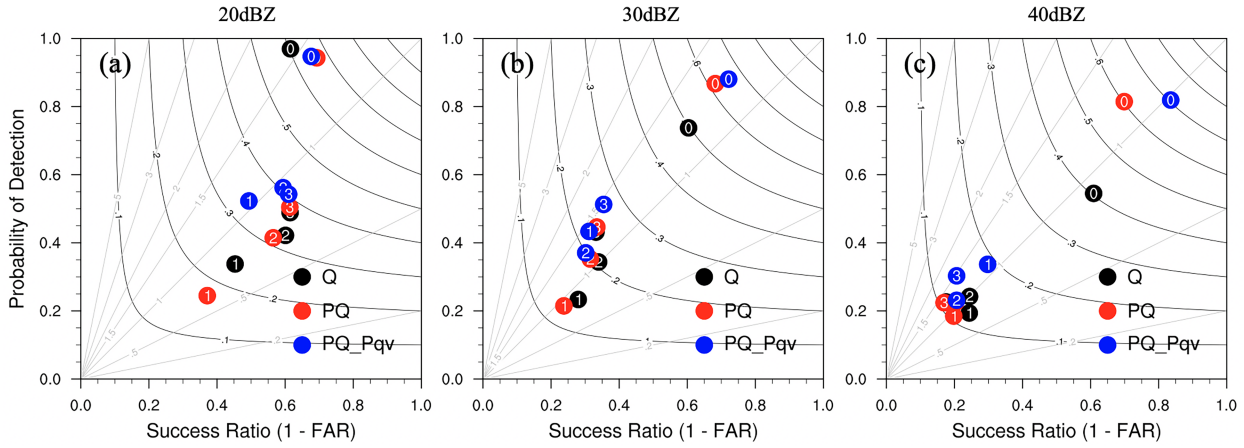

FIG. 6. Performance diagrams for the 3-h forecasts of composite reflectivity beginning at 2300 UTC 22 May 2019 for (a) 20-, (b) 30-, and (c) 40-dBZ thresholds. The black curves represent the critical success index (CSI), and the diagonal gray lines represent the bias. The number in the dots is the forecast length ("0" represents 0-h forecast or analysis, "1" represents 1-h forecast … etc.).

The performance diagrams for the 3-h forecasts initiated at 2200 UTC for 20-, 30-, and 40-dBZ thresholds are also plotted for this case (Fig. 11). At the analysis time, both PQ and PQ_Pqv have lower bias and higher CSI than that of Q at all thresholds, indicating evident improvement of the analysis by using the power transformation function. For the forecasts, PQ_Pqv outperforms both Q and PQ for the entire period, exhibiting the highest values of POD, SR and CSI, especially at the 1-h forecast. Both Q and PQ exhibit similar performance at the 30- and 40-dBZ thresholds (Figs. 11b,c). For the 20-dBZ threshold, PQ outperforms Q with slightly higher SR and CSI values.

The total and individual cost functions for this case are also presented (Fig. 12). It is shown that PQ and PQ_Pqv have faster convergence rates than Q, especially for the parts corresponding to radial velocity (Fig. 12b). For the normalized total cost function (Fig. 12a), Q converges faster at the first two iteration steps and PQ and PQ_Pqv converge faster for the rest of iterations. For reflectivity (Fig. 12c), Q has faster convergence rates at the first four iteration steps. Overall, however, PQ and PQ_Pqv exhibit very similar convergence rates, which reach the smallest cost function values and level off more quickly compared with Q.

c. *Quantitative verification on forecast performance for all five cases*

To more fully investigate the impact of assimilating power-transformed mixing ratios, the fractions skill scores (FSS; Roberts and Lean 2008) aggregated over all five cases are calculated at every hour for the 3-h forecasts initiated from 2000 to 2300 UTC with thresholds of 20 and 40 dBZ for Q, PQ, and PQ_Pqv (Fig. 13). Only areas where the observed reflectivity is greater than 0 dBZ are included in the calculation. At the analysis time, the averaged FSS values for PQ and PQ_Pqv are much higher than that for Q for all thresholds, which indicates that using power-transformed mixing ratios as

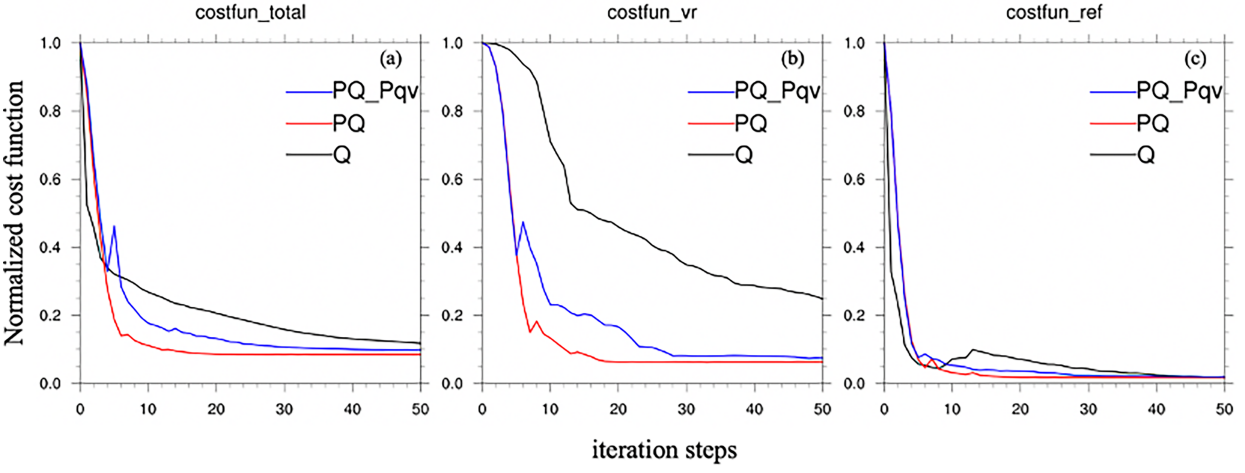

FIG. 7. The normalized (left) total, (center) radial velocity, and (right) reflectivity cost functions for Q, PQ, and PQ_Pqv for the analysis at 1900 UTC 22 May 2019.

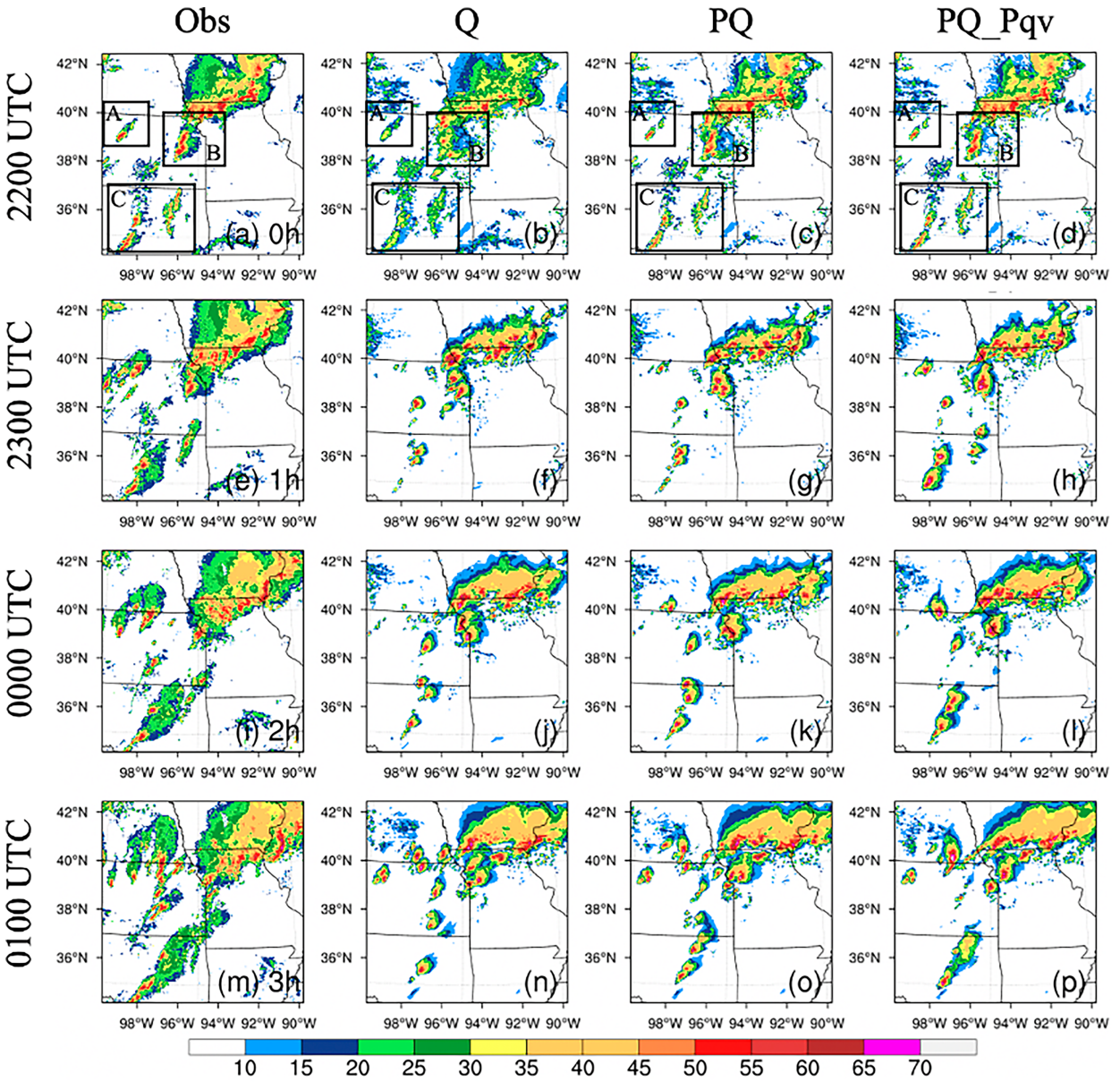

FIG. 8. As in Fig. 3, but initiated at 2200 UTC 28 May 2019.

control variables greatly improves the analysis. Additionally, PQ_Pqv outperforms PQ with higher FSS values at the analysis time. Although the power transformation of hydrometeor mixing ratios is beneficial for the analysis, its impact on the prediction is much smaller. The FSS values for the entire 3-h forecast are quite similar for Q and PQ, except for the 1-h forecast at the 20-dBZ threshold (Fig. 13a). However, the averaged FSSs of PQ_Pqv remain superior during the entire forecast period compared to Q and PQ. This indicates the positive impact of assimilating pseudo–water vapor on the short-term severe weather forecasts. In general, applying power transformations to the hydrometeor and water vapor mixing ratios provides the best forecast performance for the five cases, which is consistent with the forecasted composite reflectivity fields analyzed in the above two individual case studies.

Given that the relative performance of each experiment may be different between the five cases, it is useful to investigate variability among the five cases. The performance diagram for 3-h composite reflectivity forecasts shows that the 20 May 2019 case is the best-performing case in terms of CSI, POD, and SR for both the 20- and 40-dBZ thresholds, while the 28 May 2019 case has the least biases (Fig. 14). On the other hand, the 22 May 2019 case is the worst-performing case based on SR and CSI, while the 17 May 2019 case is the worst-performing case in terms of POD for both thresholds.

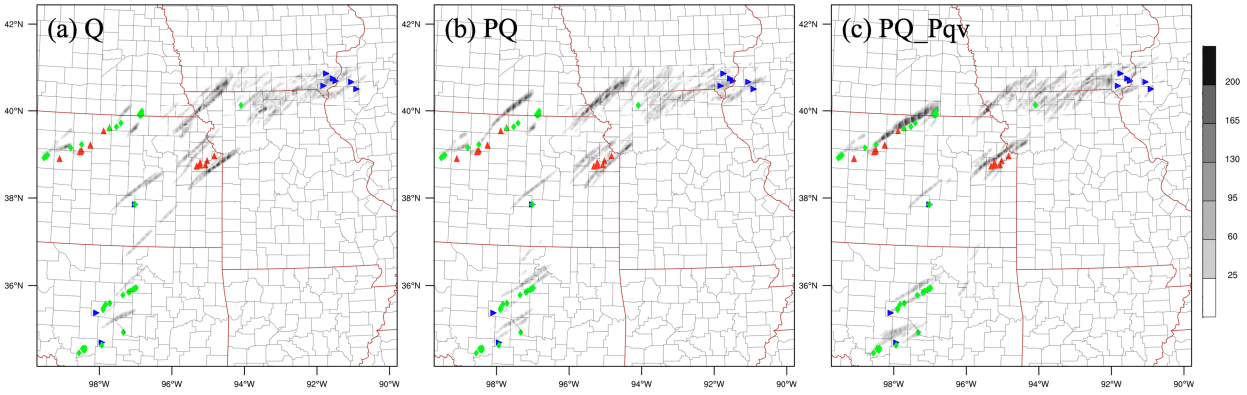

FIG. 9. As in Fig. 4, but initiated at 2200 UTC 28 May 2019.

Score metrics for all real cases indicate PQ_Pqv has the best 3-h forecast performance, except for the 17 May 2019 case for the 20-dBZ threshold and the 23 May 2019 case for the 40-dBZ threshold. In addition, the forecast skill of all cases exhibits more variability at the 40-dBZ threshold than at the lower 20-dBZ threshold (Fig. 14a versus Fig. 14b).

To quantitatively evaluate the predictive skill for precipitation using different control variables, FSS values of 1-h

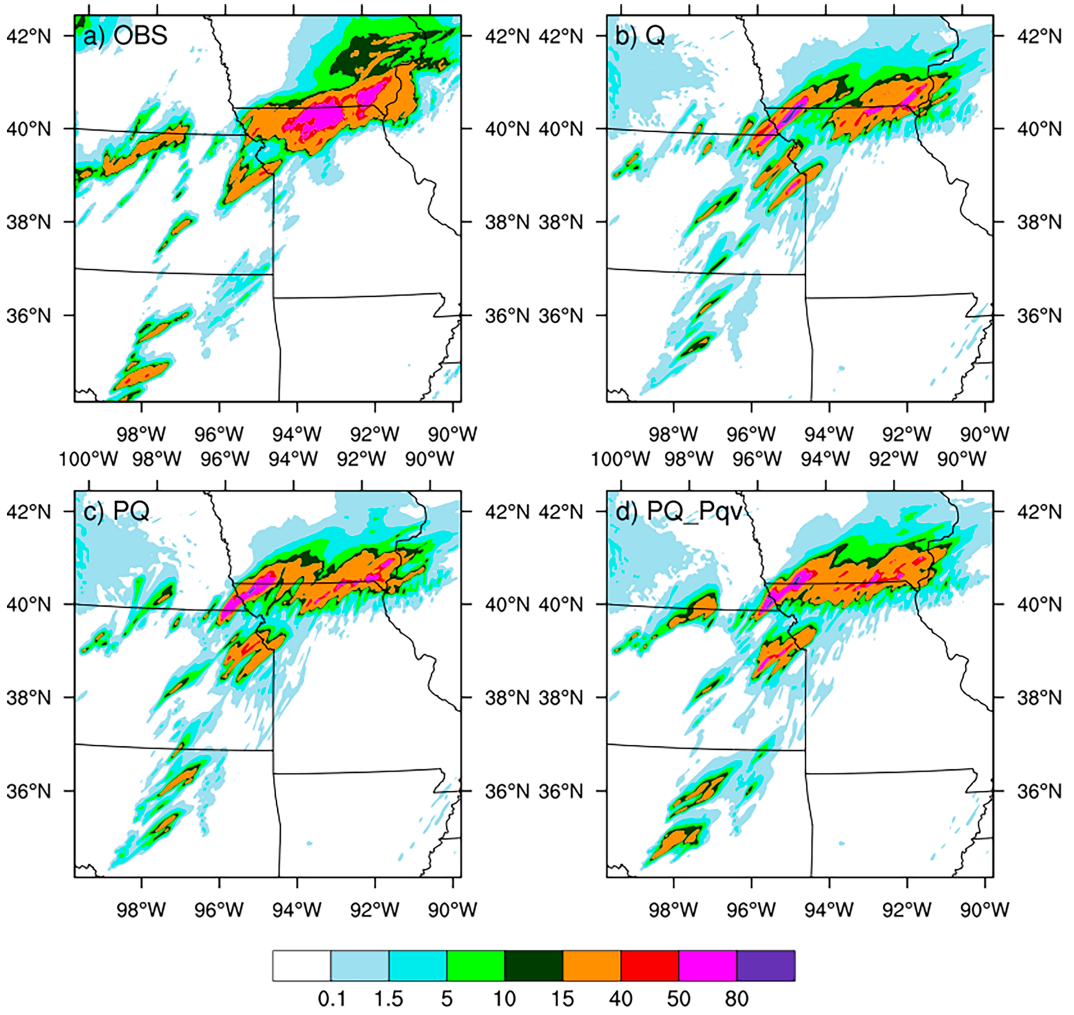

FIG. 10. As in Fig. 5, but initiated at 2200 UTC 28 May 2019.

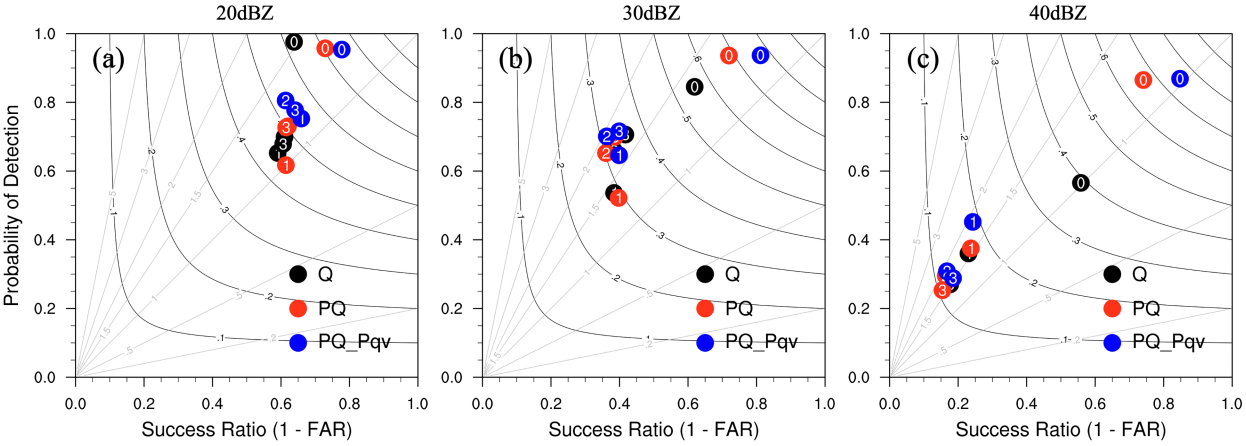

FIG. 11. As in Fig. 6, but initiated at 2200 UTC 28 May 2019.

accumulated precipitation for Q, PQ, and PQ_Pqv averaged over all five real data cases with different thresholds (1.0, 2.5, 5.0, and 10.0 mm) are also calculated (Fig. 15). The precipitation forecasts are verified against the NCEP Stage-IV precipitation dataset (Du 2011). For the 0–1-h forecast (Fig. 15a), PQ and PQ_Pqv have relatively higher scores for all thresholds than Q. Moreover, PQ_Pqv outperforms PQ with the highest FSS values. For the 1–2-h forecast (Fig. 15b), Q and PQ show similar FSS values for all thresholds, while PQ_Pqv presents slightly higher scores at the 1.0-, 2.5- and 5-mm thresholds. By the 2–3-h forecast (Fig. 15c), all three experiments show very similar FSS values. However, PQ_Pqv produces slightly lower scores compared with Q and PQ at the 5- and 10-mm thresholds. In summary, using power-transformed hydrometeor mixing ratios as control variables exhibits better quantitative precipitation prediction forecast (QPF) skill, especially during the 0–1-h forecast. Additionally, this improvement is more obvious when using both power-transformed hydrometeor and water vapor mixing ratios as control variables.

5. Conclusions

In this study, the impact of using power-transformed hydrometeor and water vapor mixing ratios as control variables on short-term convective-scale forecasts is tested within the 3DVAR system developed for the NSSL WoF project (Gao et al. 2013). Five severe weather cases of 17, 20, 22, 23, and 28 May 2019 are tested to investigate whether the above strategy can help improve the efficiency and accuracy of radar reflectivity DA and convective-scale short-term severe weather forecasts.

Three experiments—Q, PQ, and PQ_Pqv—are compared to test the impact of the power transformation function applied to water-related mixing ratios as control variables on short-term severe weather forecasts. Detailed analyses of two of the real data cases is performed. At the analysis time, the composite reflectivity (and by proxy the storm intensity) differs for each experiment. Convective cells in PQ and PQ_Pqv which use the power transformation function are stronger compared with Q, which does not use the power transformation function, and are in better agreement with the observed

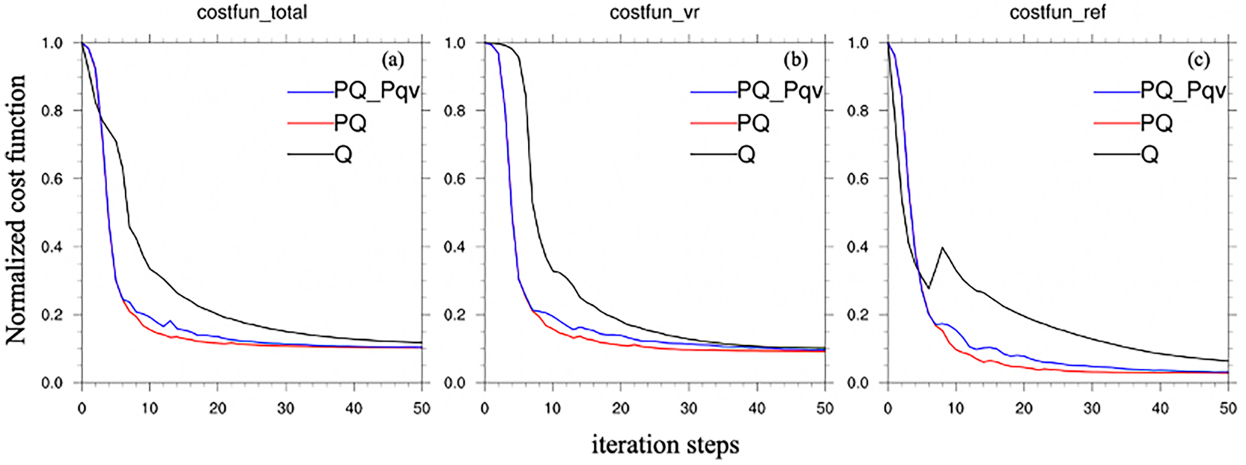

FIG. 12. As in Fig. 7, but for 28 May 2019.

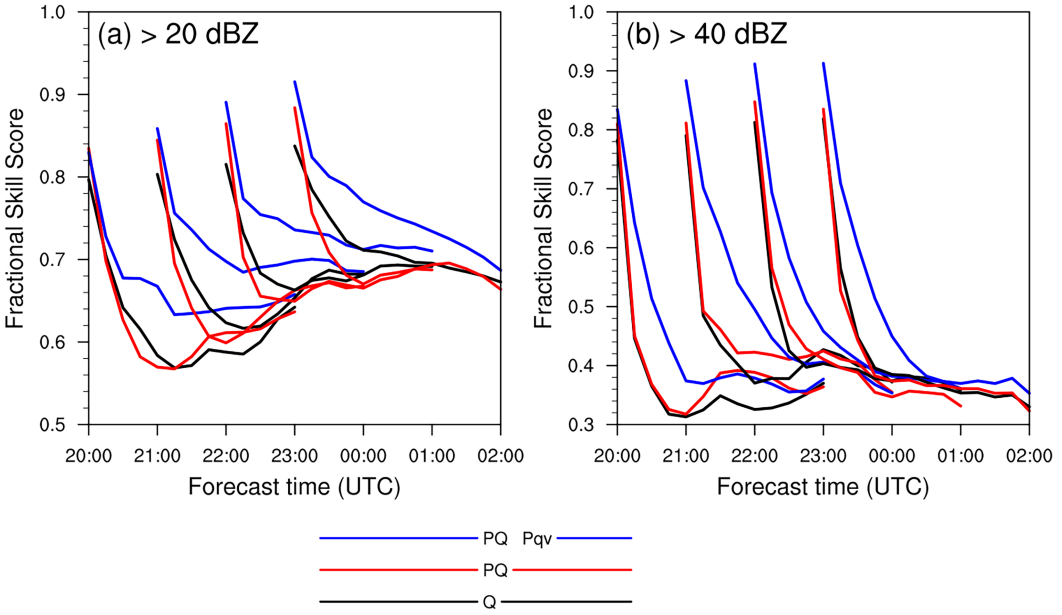

FIG. 13. Fractional skill scores of the 0–3-h composite reflectivity forecasts for (a) 20- and (b) 40-dBZ thresholds within the entire forecast cycle aggregated over all five cases. The output frequency is 15 min.

composite reflectivity. In addition, some spurious cells produced in Q for two cases are comparatively reduced in PQ and PQ_Pqv. For the 3-h forecasts, PQ_Pqv, which uses the power-transform function for both hydrometeors and water vapor as control variables, gives the best forecast, especially during the first hour of the forecast. The UH swaths for the 3-h forecasts show that the forecast UH tracks are similar for all three experiments. However, the predicted UH tracks in some regions are more consistent with the observations for PQ_Pqv with smaller phase errors and stronger intensity compared with the other two experiments. The performance diagrams represent the overall performance of the analysis and forecast. At the analysis time, PQ produces higher CSI and SR for reflectivity compared to Q at all thresholds. For the 1–3-h forecasts, Q and PQ exhibit similar performance for most thresholds. PQ_Pqv outperforms both experiments for the entire forecast period. The individual (i.e., radial velocity and reflectivity) and total cost functions are normalized to compare the convergence rates. Both PQ and PQ_Pqv have faster convergence rates than Q, with smaller cost function

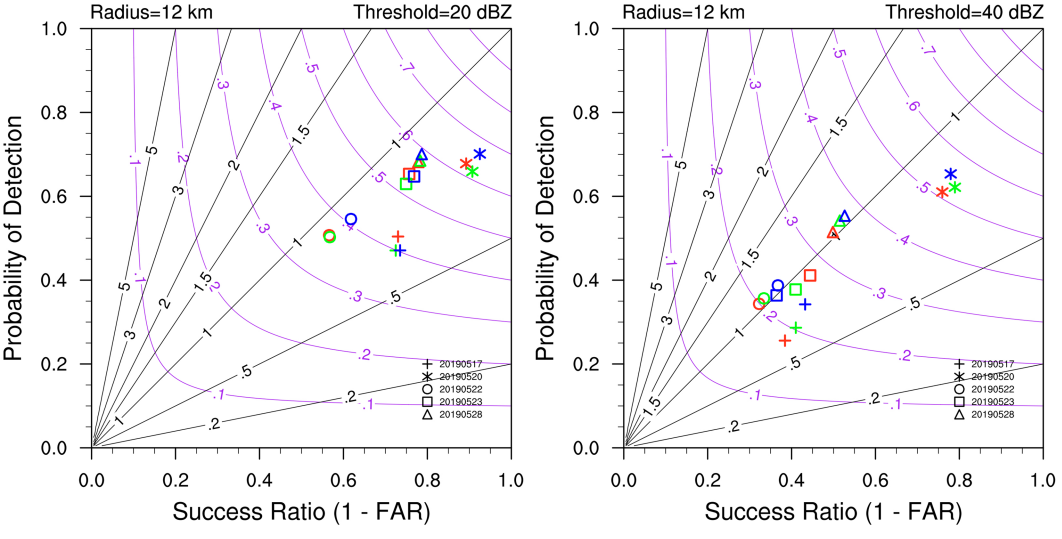

FIG. 14. Performance diagrams for 3-h composite reflectivity forecasts for each case and experiment relative to MRMS composite reflectivity observations at thresholds of (left) 20 and (right) 40 dBZ with a neighborhood radius of 12 km. Red, green, and blue colors denote the experiments Q, PQ, and PQ_Pqv, respectively.

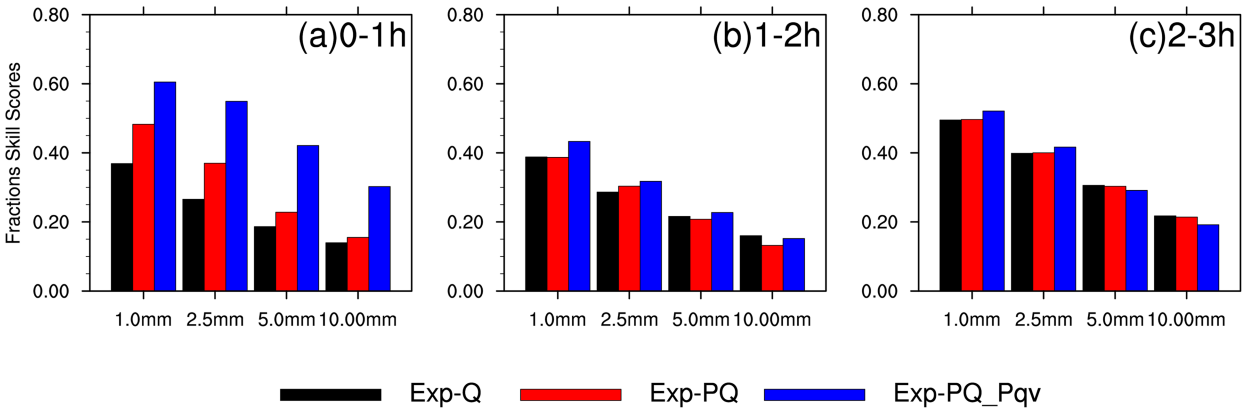

FIG. 15. The FSSs of 1-h accumulated precipitation for (a) 0–1 h, (b) 1–2 h, and (c) 2–3 h with different thresholds for Q, PQ, and PQ_Pqv averaged over all five cases.

values during most of the minimization process, indicating the higher efficiency achieved by using power-transformed control variables.

Quantitative verification over all five cases indicates that both PQ and PQ_Pqv outperform Q with higher FSS scores at analysis time. More broadly, PQ_Pqv has the highest FSS values for both reflectivity and QPF compared with Q and PQ at most forecast times, indicating the positive impact of additionally applying the power transformation to water vapor mixing ratios and the assimilation of pseudo–water vapor observations.

In the future, more cases will be tested to see if the strategies explored in this study are representative. Furthermore, the power transformation function can be used in a hybrid ensemble or hybrid ensemble and variational system. The ensemble information may help make the analysis more balanced among different model variables and may also further improve short-term severe weather analyses and forecasts.

Acknowledgments. This work was supported by NOAA/Office of Oceanic and Atmospheric Research under the NOAA–University of Oklahoma Cooperative Agreements NA16OAR4320115 and NA21OAR4320204, U.S. Department of Commerce. The work was also partially supported by the National Science Foundation Grant AGS-2136161. Computing resources were provided by OU Supercomputing Center for Education and Research (OSCER).

Data availability statement. The source codes of the WRF Model version 3.7.1 can be downloaded after providing an email address at the following website (https://www2.mmm.ucar.edu/wrf/users/download/get_source.html). The Multi-Radar Multi-Sensor (MRMS) and the Stage-IV rainfall products, and the aggregate forecast statistics for composite reflectivity and APCP are accessible online (https://doi.org/10.5281/zenodo.4495919).

REFERENCES

Carley, J. R., 2012: Hybrid ensemble-3DVar radar data assimilation for the short-term prediction of convective storms. Ph.D. dissertation, Purdue University, 206 pp.

Carlin, J. T., J. Gao, J. C. Snyder, and A. V. Ryzhkov, 2017: Assimilation of Z_{DR} columns for improving the spinup and forecast of convective storms in storm-scale models: Proof-of-concept experiments. *Mon. Wea. Rev.*, **145**, 5033–5057, https://doi.org/10.1175/MWR-D-17-0103.1.

Caya, A., J. Sun, and C. Snyder, 2005: A comparison between the 4DVAR and the ensemble Kalman filter techniques for radar data assimilation. *Mon. Wea. Rev.*, **133**, 3081–3094, https://doi.org/10.1175/MWR3021.1.

Chen, L., C. Liu, M. Xue, G. Zhao, R. Kong, and Y. Jung, 2021: Use of power transform mixing ratios as hydrometeor control variables for direct assimilation of radar reflectivity in GSI En3DVar and tests with five convective storm cases. *Mon. Wea. Rev.*, **149**, 645–659, https://doi.org/10.1175/MWR-D-20-0149.1.

Clark, A., and Coauthors, 2020: A real-time, simulated forecasting experiment for advancing the prediction of hazardous convective weather. *Bull. Amer. Meteor. Soc.*, **101**, E2022–E2024, https://doi.org/10.1175/BAMS-D-19-0298.1.

Courtier, P., 1997: Dual formulation of four-dimensional variational assimilation. *Quart. J. Roy. Meteor. Soc.*, **123**, 2449–2461, https://doi.org/10.1002/qj.49712354414.

——, J.-N. Thépaut, and A. Hollingsworth, 1994: A strategy for operational implementation of 4D-Var, using an incremental approach. *Quart. J. Roy. Meteor. Soc.*, **120**, 1367–1387, https://doi.org/10.1002/qj.49712051912.

Doviak, R. J., and D. S. Zrnić, 1993: *Doppler Radar and Weather Observations.* 2nd ed. Academic Press, 562 pp.

Dowell, D. C., L. J. Wicker, and C. Snyder, 2011: Ensemble Kalman filter assimilation of radar observations of the 8 May 2003 Oklahoma City supercell: Influences of reflectivity observations on storm-scale analyses. *Mon. Wea. Rev.*, **139**, 272–294, https://doi.org/10.1175/2010MWR3438.1.

Du, J., 2011: NCEP/EMC 4KM Gridded Data (GRIB) Stage IV data, version 1.0. UCAR/NCAR–Earth Observing Laboratory, accessed 17 September 2023, https://doi.org/10.5065/D6PG1QDD.

Gao, J., and M. Xue, 2008: An efficient dual-resolution approach for ensemble data assimilation and tests with simulated Doppler radar data. *Mon. Wea. Rev.*, **136**, 945–963, https://doi.org/10.1175/2007MWR2120.1.

——, and D. J. Stensrud, 2012: Assimilation of reflectivity data in a convective-scale, cycled 3DVAR framework with hydrometeor classification. *J. Atmos. Sci.*, **69**, 1054–1065, https://doi.org/10.1175/JAS-D-11-0162.1.

——, M. Xue, A. Shapiro, and K. K. Droegemeier, 1999: A variational method for the analysis of three-dimensional wind fields from two Doppler radars. *Mon. Wea. Rev.*, **127**, 2128–2142, https://doi.org/10.1175/1520-0493(1999)127<2128:AVMFTA>2.0.CO;2.

——, ——, ——, Q. Xu, and K. K. Droegemeier, 2001: Three-dimensional simple adjoint velocity retrievals from single-Doppler radar. *J. Atmos. Oceanic Technol.*, **18**, 26–38, https://doi.org/10.1175/1520-0426(2001)018<0026:TDSAVR>2.0.CO;2.

——, ——, K. Brewster, and K. K. Droegemeier, 2004: A three-dimensional variational data analysis method with recursive filter for Doppler radars. *J. Atmos. Oceanic Technol.*, **21**, 457–469, https://doi.org/10.1175/1520-0426(2004)021<0457:ATVDAM>2.0.CO;2.

——, and Coauthors, 2013: A real-time weather-adaptive 3DVAR analysis system for severe weather detections and warnings. *Wea. Forecasting*, **28**, 727–745, https://doi.org/10.1175/WAF-D-12-00093.1.

——, C. Fu, D. J. Stensrud, and J. S. Kain, 2016: OSSEs for an ensemble 3DVAR data assimilation system with radar observations of convective storms. *J. Atmos. Sci.*, **73**, 2403–2426, https://doi.org/10.1175/JAS-D-15-0311.1.

Gilmore, M. S., J. M. Straka, and E. N. Rasmussen, 2004: Precipitation uncertainty due to variations in precipitation particle parameters within a simple microphysics scheme. *Mon. Wea. Rev.*, **132**, 2610–2627, https://doi.org/10.1175/MWR2810.1.

Hong, S.-Y., Y. Noh, and J. Dudhia, 2006: A new vertical diffusion package with an explicit treatment of entrainment processes. *Mon. Wea. Rev.*, **134**, 2318–2341, https://doi.org/10.1175/MWR3199.1.

Hu, M., M. Xue, and K. Brewster, 2006a: 3DVAR and cloud analysis with WSR-88D Level-II data for the prediction of the Fort Worth, Texas, tornadic thunderstorms. Part I: Cloud analysis and its impact. *Mon. Wea. Rev.*, **134**, 675–698, https://doi.org/10.1175/MWR3092.1.

——, ——, J. Gao, and K. Brewster, 2006b: 3DVAR and cloud analysis with WSR-88D Level-II data for the prediction of the Fort Worth, Texas, tornadic thunderstorms. Part II: Impact of radial velocity analysis via 3DVAR. *Mon. Wea. Rev.*, **134**, 699–721, https://doi.org/10.1175/MWR3093.1.

Iacono, M. J., J. S. Delamere, E. J. Mlawer, M. W. Shephard, S. A. Clough, and W. D. Collins, 2008: Radiative forcing by long-lived greenhouse gases: Calculations with the AER radiative transfer models. *J. Geophys. Res.*, **113**, D13103, https://doi.org/10.1029/2008JD009944.

Johnson, A., X. Wang, J. R. Carley, L. J. Wicker, and C. Karstens, 2015: A comparison of multiscale GSI-based EnKF and 3DVar data assimilation using radar and conventional observations for midlatitude convective-scale precipitation forecasts. *Mon. Wea. Rev.*, **143**, 3087–3108, https://doi.org/10.1175/MWR-D-14-00345.1.

Jung, Y., M. Xue, G. Zhang, and J. M. Straka, 2008: Assimilation of simulated polarimetric radar data for a convective storm using the ensemble Kalman filter. Part II: Impact of polarimetric data on storm analysis. *Mon. Wea. Rev.*, **136**, 2246–2260, https://doi.org/10.1175/2007MWR2288.1.

Lai, A., J. Gao, S. E. Koch, Y. Wang, S. Pan, A. O. Fierro, C. Cui, and J. Min, 2019: Assimilation of radar radial velocity, reflectivity, and pseudo–water vapor for convective-scale NWP in a variational framework. *Mon. Wea. Rev.*, **147**, 2877–2900, https://doi.org/10.1175/MWR-D-18-0403.1.

Li, H., C. Liu, M. Xue, J. Park, L. Chen, Y. Jung, R. Kong, and C.-C. Tong, 2022: Use of power transform total number concentration as control variable for direct assimilation of radar reflectivity in GSI En3DVar and tests with six convective storms cases. *Mon. Wea. Rev.*, **150**, 821–842, https://doi.org/10.1175/MWR-D-21-0041.1.

Li, Y., I. M. Navon, W. Yang, X. Zou, J. R. Bates, S. Moorthi, and R. W. Higgins, 1994: Four-dimensional variational data assimilation experiments with a multilevel semi-Lagrangian semi-implicit general circulation model. *Mon. Wea. Rev.*, **122**, 966–983, https://doi.org/10.1175/1520-0493(1994)122<0966:FDVDAE>2.0.CO;2.

Lilly, D. K., 1990: Numerical prediction of thunderstorms—Has its time come? *Quart. J. Roy. Meteor. Soc.*, **116**, 779–798, https://doi.org/10.1002/qj.49711649402.

Lin, Y.-L., R. D. Farley, and H. D. Orville, 1983: Bulk parameterization of the snow field in a cloud model. *J. Climate Appl. Meteor.*, **22**, 1065–1092, https://doi.org/10.1175/1520-0450(1983)022<1065:BPOTSF>2.0.CO;2.

Liu, C., M. Xue, and R. Kong, 2019: Direct assimilation of radar reflectivity data using 3DVAR: Treatment of hydrometeor background errors and OSSE tests. *Mon. Wea. Rev.*, **147**, 17–29, https://doi.org/10.1175/MWR-D-18-0033.1.

——, ——, and ——, 2020: Direct variational assimilation of radar reflectivity and radial velocity data: Issues with nonlinear reflectivity operator and solutions. *Mon. Wea. Rev.*, **148**, 1483–1502, https://doi.org/10.1175/MWR-D-19-0149.1.

Lorenc, A. C., 1986: Analysis methods for numerical weather prediction. *Quart. J. Roy. Meteor. Soc.*, **112**, 1177–1194, https://doi.org/10.1002/qj.49711247414.

Navon, I. M., and D. M. Legler, 1987: Conjugate-gradient methods for large-scale minimization in meteorology. *Mon. Wea. Rev.*, **115**, 1479–1502, https://doi.org/10.1175/1520-0493(1987)115<1479:CGMFLS>2.0.CO;2.

Roberts, N. M., and H. W. Lean, 2008: Scale-selective verification of rainfall accumulations from high-resolution forecasts of convective events. *Mon. Wea. Rev.*, **136**, 78–97, https://doi.org/10.1175/2007MWR2123.1.

Roebber, P. J., 2009: Visualizing multiple measures of forecast quality. *Wea. Forecasting*, **24**, 601–608, https://doi.org/10.1175/2008WAF2222159.1.

Ryzhkov, A., M. Pinsky, A. Pokrovsky, and A. Khain, 2011: Polarimetric radar observation operator for a cloud model with spectral microphysics. *J. Appl. Meteor. Climatol.*, **50**, 873–894, https://doi.org/10.1175/2010JAMC2363.1.

Smith, P. L., C. G. Myers, and H. D. Orville, 1975: Radar reflectivity factor calculations in numerical cloud models using bulk parameterization of precipitation. *J. Appl. Meteor.*, **14**, 1156–1165, https://doi.org/10.1175/1520-0450(1975)014<1156:RRFCIN>2.0.CO;2.

Smith, T. M., and Coauthors, 2016: Multi-Radar Multi-Sensor (MRMS) severe weather and aviation products: Initial operating capabilities. *Bull. Amer. Meteor. Soc.*, **97**, 1617–1630, https://doi.org/10.1175/BAMS-D-14-00173.1.

Stensrud, D. J., and J. Gao, 2010: Importance of horizontally inhomogeneous environmental initial conditions to ensemble storm-scale radar data assimilation and very short-range forecasts. *Mon. Wea. Rev.*, **138**, 1250–1272, https://doi.org/10.1175/2009MWR3027.1.

Sun, J., and N. A. Crook, 1997: Dynamical and microphysical retrieval from Doppler radar observations using a cloud model and its adjoint. Part I: Model development and simulated data experiments. *J. Atmos. Sci.*, **54**, 1642–1661, https://doi.org/10.1175/1520-0469(1997)054<1642:DAMRFD>2.0.CO;2.

——, and H. Wang, 2013: Radar data assimilation with WRF 4D-Var. Part II: Comparison with 3D-Var for a squall line over the U.S. Great Plains. *Mon. Wea. Rev.*, **141**, 2245–2264, https://doi.org/10.1175/MWR-D-12-00169.1.

Tewari, M., and Coauthors, 2004: Implementation and verification of the united Noah land surface model in the WRF model. *20th Conf. on Weather Analysis and Forecasting/16th Conf. on Numerical Weather Prediction*, Seattle, WA, Amer. Meteor. Soc., 14.2a, https://ams.confex.com/ams/84Annual/techprogram/paper_69061.htm.

Thompson, G., P. R. Field, R. M. Rasmussen, and W. D. Hall, 2008: Explicit forecasts of winter precipitation using an improved bulk microphysics scheme. Part II: Implementation of a new snow parameterization. *Mon. Wea. Rev.*, **136**, 5095–5115, https://doi.org/10.1175/2008MWR2387.1.

Tong, M., and M. Xue, 2005: Ensemble Kalman filter assimilation of Doppler radar data with a compressible nonhydrostatic model: OSS experiments. *Mon. Wea. Rev.*, **133**, 1789–1807, https://doi.org/10.1175/MWR2898.1.

Wang, H., J. Sun, X. Zhang, X.-Y. Huang, and T. Auligné, 2013: Radar data assimilation with WRF 4D-Var. Part I: System development and preliminary testing. *Mon. Wea. Rev.*, **141**, 2224–2244, https://doi.org/10.1175/MWR-D-12-00168.1.

Wang, Y., and X. Wang, 2017: Direct assimilation of radar reflectivity without tangent linear and adjoint of the nonlinear observation operator in the GSI-based EnVar system: Methodology and experiment with the 8 May 2003 Oklahoma City tornadic supercell. *Mon. Wea. Rev.*, **145**, 1447–1471, https://doi.org/10.1175/MWR-D-16-0231.1.

——, J. Gao, P. S. Skinner, K. Knopfmeier, T. Jones, G. Creager, P. L. Heiselman, and L. J. Wicker, 2019: Test of a weather-adaptive dual-resolution hybrid Warn-on-Forecast analysis and forecast system for several severe weather events. *Wea. Forecasting*, **34**, 1807–1827, https://doi.org/10.1175/WAF-D-19-0071.1.

Wheatley, D. M., K. H. Knopfmeier, T. A. Jones, and G. J. Creager, 2015: Storm-scale data assimilation and ensemble forecasting with the NSSL experimental Warn-on-Forecast System. Part I: Radar data experiments. *Wea. Forecasting*, **30**, 1795–1817, https://doi.org/10.1175/WAF-D-15-0043.1.

Xiao, Q., Y. Kuo, J. Sun, W. Lee, D. M. Barker, and E. Lim, 2007: An approach of radar reflectivity data assimilation and its assessment with the inland QPF of Typhoon Rusa (2002) at landfall. *J. Appl. Meteor. Climatol.*, **46**, 14–22, https://doi.org/10.1175/JAM2439.1.

Yang, R., R. J. Purser, J. R. Carley, M. Pondeca, Y. Zhu, and S. Levine, 2020: Application of a nonlinear transformation function to the variational analysis of visibility and ceiling height. NCEP Office Note 502, 38 pp., https://doi.org/10.25923/ESW8-5N84.

Yussouf, N., E. R. Mansell, L. J. Wicker, D. M. Wheatley, and D. J. Stensrud, 2013: The ensemble Kalman filter analyses and forecasts of the 8 May 2003 Oklahoma City tornadic supercell storm using single- and double-moment microphysics schemes. *Mon. Wea. Rev.*, **141**, 3388–3412, https://doi.org/10.1175/MWR-D-12-00237.1.

Zhang, G., 2017: *Weather Radar Polarimetry.* CRC Press and Taylor & Francis Group, 304 pp.

——, J. Gao, and M. Du, 2021: Parameterized forward operators for simulation and assimilation of polarimetric radar data with numerical weather predictions. *Adv. Atmos. Sci.*, **38**, 737–754, https://doi.org/10.1007/s00376-021-0289-6.

Zhao, J., J. Gao, T. A. Jones, and J. Hu, 2021: Impact of assimilating high-resolution atmospheric motion vectors on convective scale short-term forecasts. 1: Observing System Simulation Experiment (OSSE). *J. Adv. Model. Earth Syst.*, **13**, e2021MS002484, https://doi.org/10.1029/2021MS002484.